











Non-collinear and asymmetric polar moments at back-gated SrTiO₃ interfaces

Fryderyk Lyzwa¹[✉], Yurii G. Pashkevich²², Premysl Marsik¹¹, Andrei Sirenko³, Andrew Chan⁴, Benjamin P. P. Mallett^{4,5}, Meghdad Yazdi-Rizi¹, Bing Xu¹, Luis M. Vicente-Arche⁶, Diogo C. Vaz⁶⁶, Gervasi Herranz⁷⁷, Maximilien Cazayous⁸, Pierre Hemme⁸, Katrin Fürsich⁹⁹, Matteo Minola⁹⁹, Bernhard Keimer⁹⁹, Manuel Bibes⁶⁶ & Christian Bernhard¹¹[✉]

The mechanism of the gate-field-induced metal-to-insulator transition of the electrons at the interface of SrTiO₃ with LaAlO₃ or AlO_x is of great current interest. Here, we show with infrared ellipsometry and confocal Raman spectroscopy that an important role is played by a polar lattice distortion that is non-collinear, highly asymmetric and hysteretic with respect to the gate field. The anomalous behavior and the large lateral component of the underlying local electric field is explained in terms of the interplay between the oxygen vacancies, that tend to migrate and form extended clusters at the antiferrodistortive domain boundaries, and the interfacial electrons, which get trapped/detrapped at the oxygen vacancy clusters under a positive/negative gate bias. Our findings open new perspectives for the defect engineering of lateral devices with strongly enhanced and hysteretic local electric fields that can be manipulated with various parameters, like strain, temperature, or photons.

¹Department of Physics and Fribourg Center for Nanomaterials, University of Fribourg, Chemin du Musée 3, CH-1700 Fribourg, Switzerland. ²O. O. Galkin Donetsk Institute for Physics and Engineering NAS of Ukraine, UA-03028 Kyiv, Ukraine. ³Department of Physics, New Jersey Institute of Technology, Newark, NJ 07102, USA. ⁴School of Chemical Sciences and the MacDiarmid Institute for Advanced Materials and Nanotechnology, The University of Auckland, Auckland, New Zealand. ⁵Robinson Research Institute, Victoria University of Wellington, 69 Gracefield Rd., Lower Hutt 5010, New Zealand. ⁶Unité Mixte de Physique, CNRS, Thales, Université Paris-Saclay, 91767 Palaiseau, France. ⁷Institut de Ciència de Materials de Barcelona (ICMAB-CSIC), Campus UAB, 08193 Bellaterra, Catalonia, Spain. ⁸Laboratoire Matériaux et Phénomènes Quantiques (UMR 7162 CNRS), Université Paris Cité, 75205 Paris, Cedex 13, France. ⁹Max-Planck-Institut für Festkörperforschung, Heisenbergstrasse 1, 70569 Stuttgart, Germany. ✉email: fryderyk.lyzwa@unifr.ch; christian.bernhard@unifr.ch

At room temperature, SrTiO₃ (STO) exhibits a cubic perovskite structure and a band-insulating electronic ground state with an energy gap of 3.25 eV^{1,2}. Its macroscopic properties are typical for this class of materials, except for mobile oxygen vacancies which make it an interesting ion conductor³. At $T^* = 105$ K, STO undergoes an antiferrodistortive (AFD) transition into a tetragonal state that arises from an antiphase rotation of the TiO₆ octahedra around the tetragonal axis^{4,5}. If no preferred direction is imposed, e.g. by applying external pressure or electric fields, a multi-domain state develops for which the tetragonal axis is either along the x-, y-, or z-direction of the perovskite structure. The resulting AFD domain boundaries are strained and tend to be attractive for oxygen vacancies and become ferroelastic and even polar^{6–9}.

Below about 50 K, the dielectric properties of STO become highly anomalous as it approaches a ferroelectric instability that is avoided only by the quantum fluctuations of the lattice¹⁰. This quantum paraelectric regime is characterized by a divergence of the dielectric constant toward giant low-temperature values of up to $\epsilon_0 \approx 20,000$ that is caused by an anomalously strong softening of the lowest infrared-active transverse phonon (TO₁ mode) (see e.g.^{11,12} and Supplementary Fig. 2). This so-called ‘soft mode’ involves the off-center displacement of the titanium ions with respect to the surrounding octahedron of oxygen ions, which, in the static limit, represents the ferroelectric (FE) order parameter. The FE order can be readily induced, e.g. by isoelectronic cation substitution in Sr_{1-x}Ca_xTiO₃^{13,14}, via strain from a lattice mismatch with the substrate in thin films¹⁵, by external pressure¹⁶, by electric fields in excess of 2 kV/cm¹⁷, and even by replacing the oxygen isotope ¹⁶O with ¹⁸O¹⁸. The large ϵ_0 values can also enhance flexoelectric effects for which strain gradients give rise to a polar moment¹⁹.

More recently, heterostructures and devices based on STO have received considerable attention thanks to a great general interest in the electronic conduction along oxide-based interfaces and domain boundaries²⁰ as well as on the effect of oxygen intercalation on the electronic properties of metal-oxide thin films and devices, especially in the context of liquid ion gating²¹. In particular, the interface of STO with LaAlO₃ (LAO) or AlO_x has been intensively studied because it hosts highly mobile and even superconducting electrons (below ~ 0.3 K²²) that are very susceptible to electric field gating^{22–27}. The field-gating even allows tuning of the spin-orbit Rashba coupling and thus of spin-charge interconversion effects^{28–30}. The origin of the confined electrons and the mechanism(s) underlying the efficient field-gating are still debated.

For LAO/STO heterostructures, the polarity of the stacking of the SrO⁰/TiO₂⁰/LaO⁺/AlO₂⁻ layers causes a diverging electric potential with increasing LAO layer thickness, which can lead to an electronic reconstruction in terms of an electron transfer from the LAO to the STO layer (‘polar catastrophe’ scenario)^{24,25}. An alternative (or additional) mechanism involves oxygen vacancies in the vicinity of the interface that have a low ionization energy, since ϵ_0 is very large^{31,32}. The latter mechanism is expected to dominate in AlO_x/STO, which has no intrinsic polar discontinuity^{27–29,33}. Details on the sample growth and characterization of this study can be found in Supplementary Note 1.

Here, we show with infrared ellipsometry and confocal Raman spectroscopy that for both LAO/STO(001) and AlO_x/STO(001) a vertical gate voltage (V) induces anomalous polar moments in the vicinity of the interface which are non-collinear and strongly asymmetric with respect to the nominal electric gate field. Our data indicate that the structural domain boundaries act as conduits of oxygen interstitials and trapped charge carriers, and thus generate large local electric fields that can greatly affect the performance of oxide devices and give rise to new functionalities.

Results

Infrared ellipsometry. In infrared ellipsometry on electric-field-gated STO-based devices, an induced polar moment is manifested in characteristic changes of some of the phonon modes. This is shown in Fig. 1a–d for the so-called R-mode at 438 cm⁻¹ in AlO_x/STO, which exhibits a characteristic splitting at negative voltages. The R-mode becomes weakly infrared-active in the tetragonal state below $T^* = 105$ K (already at 0 V), where the anti-phase rotation of the neighboring TiO₆ octahedra leads to a backfolding from the R-point of the cubic Brillouin-zone and a mixing with the antiferroelectric displacement of the Ti ions^{7,34} as described in Supplementary Note 3. In the presence of an electric-field-induced polar moment, **P**, caused by a static off-center displacement of the Ti ions, this R-mode develops a second peak (colored arrows) that is redshifted and gains spectral weight at the expense of the unshifted peak.

Figure 1b, d show the gate-voltage loops of the magnitude of the peak splitting, which is strongly asymmetric and vanishes at large +V values. A corresponding R-mode splitting was previously observed in field-gated LAO/STO as well as in bulk SrTi¹⁸O₃ where the polar moment develops in the FE state below $T_{\text{Curie}} \approx 25$ K³⁵. For LAO/STO, the asymmetric gate-voltage dependence of the R-mode splitting was interpreted in terms of a built-in, vertical electric field due to the discontinuity of the polar layer stacking to which the gate field adds (is opposed) at -V (+V), such that the threshold for inducing a static polar moment is overcome (not reached). This interpretation is however challenged by our finding that this kind of R-mode splitting occurs also in AlO_x/STO for which no polar discontinuity is expected²⁷. Moreover, a detailed symmetry analysis of the infrared response of the R-mode in the presence of a polar distortion (see Supplementary Notes 3–5) suggests that the R-mode splitting can only be seen with ellipsometry if the polar moment has a sizeable horizontal component and thus is non-collinear with respect to the vertical gate field. The present results therefore indicate that additional effects are at play that govern the local electric fields and the related induced polar moments in the vicinity of the AlO_x/STO and LAO/STO interfaces.

An anomalous origin of the induced polar moments is also suggested by the unusual training and hysteresis effects of the gate-field loops of the R-mode splitting in the right panels of Fig. 1b, d. Its onset field during the first cycle (starting from the pristine state after cooling at 0 V) is strongly dependent on the sign of the variation of V. This is shown in the top panel of Fig. 1b where no R-mode splitting occurs as the voltage is first increased to +8 kV/cm, whereas it starts to develop around +2 kV/cm as the gate voltage is subsequently reduced. For the opposite cycle in the top panel of Fig. 1d, the R-mode splitting develops right away as the voltage is ramped to -V. Note that these highly asymmetric polarization and hysteresis loops are markedly different from the ones of bulk STO, for which a ferroelectric order with a symmetric hysteresis loop is induced above a threshold of about ± 2 kV/cm¹².

Complementary information about the interfacial polar moments is obtained from a related phonon anomaly at the longitudinal optical (LO₄) edge of STO around 800 cm⁻¹ that is shown in Fig. 1e, f. It arises from a transverse optical (TO) mode that is induced by the polar distortion and is infrared active only in the direction parallel to **P** (details are given in Supplementary Notes 4 and 5).

Near such an LO edge, the ellipsometric response is sensitive to both the horizontal and the vertical components of the dielectric function^{36–38} (for details see Supplementary Note 2 and 6). Accordingly, the analysis of this LO₄ anomaly yields further information about the vertical component of **P** (in addition to the one from the R-mode splitting on the horizontal component).

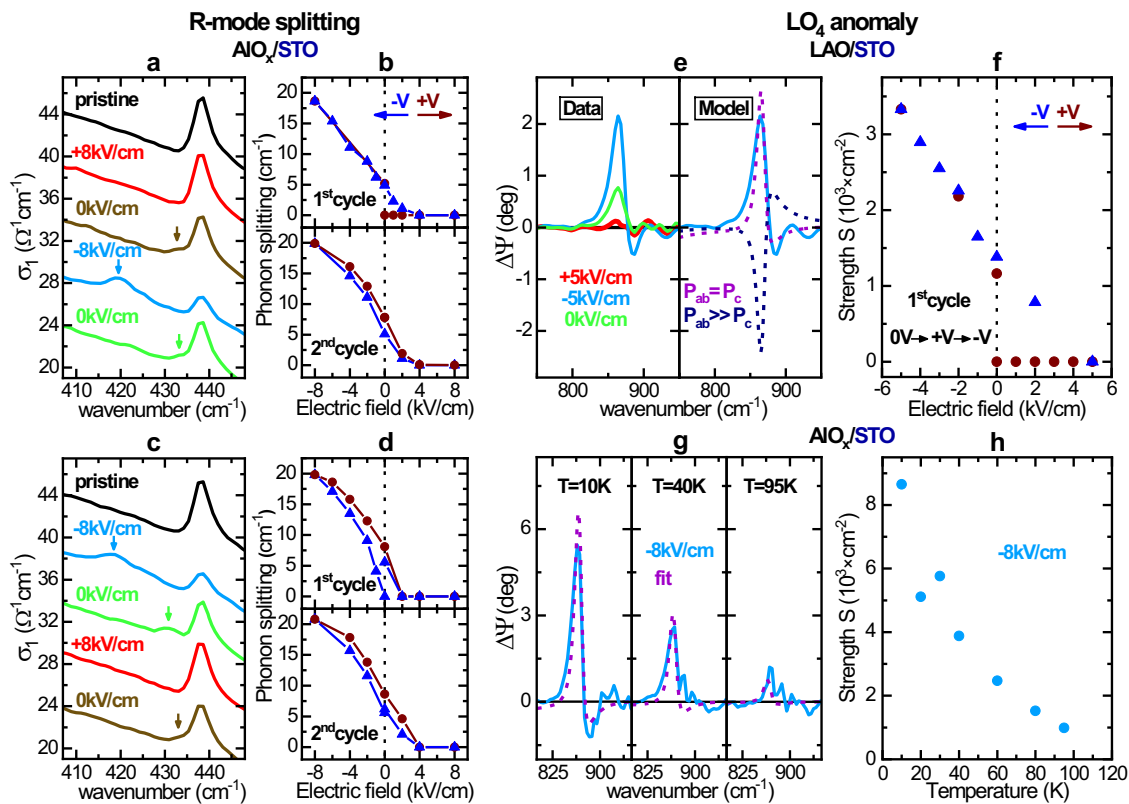


Fig. 1 Infrared ellipsometry study of phonon anomalies due to the electric-field-induced polar moment. **a** Spectra of the optical conductivity, σ_1 , showing the asymmetric R-mode splitting due to an in-plane polarization \mathbf{P}_{ab} for gate-voltage cycles $0\text{ V} \rightarrow +V \rightarrow -V$ and **b** the corresponding hysteresis loops for the magnitude of the R-mode splitting (and thus of \mathbf{P}_{ab}) at 10 K. **c** Spectra and **d** hysteresis loops of the R-mode splitting for the reverse voltage cycling direction, i.e. $0\text{ V} \rightarrow -V \rightarrow +V$. **e**, **f** Anomaly at the longitudinal optical (LO₄) edge. **e** The difference spectra of the ellipsometric angle $\Delta\Psi = \Psi_{\text{exp}} - \Psi_{0\text{V, pristine}}$ at the LO₄ edge show the signatures of an infrared-active transverse optical (TO) mode that is induced at $-V$. This new TO mode can only be modeled by assuming a polarization with a sizeable vertical component (dashed purple), instead of a polarization of pure horizontal character (dashed dark blue). **f** Corresponding voltage loops of the oscillator strength, S , of the field-induced TO mode. **g**, **h** Temperature dependence of the LO₄ anomaly. **g** Spectra of the field-induced TO mode (cyan) together with the fit (dashed purple) at selected temperatures. **h** Temperature dependence of S for the field-induced TO mode (at -8 kV/cm).

Figure 1e reveals that the LO₄ edge anomaly cannot be reproduced if \mathbf{P} only has a lateral component with $P_{ab} \gg P_c$ (dashed dark blue line), but is well described assuming that \mathbf{P} is oriented along a diagonal with respect to the surface normal with $P_{ab} = P_c$ (dashed purple line).

Figure 1f displays the gate-field loop of the amplitude of the TO mode at the LO₄ edge, as obtained with the diagonal polarization model ($P_{ab} = P_c$), which shows a similar asymmetry with respect to the gate voltage as the R-mode splitting in the top panel of Fig. 1b. This confirms the common origin of these phonon anomalies and suggests that the underlying polar moment \mathbf{P} is strongly (but not fully) inclined toward the interface. A likely scenario is that \mathbf{P} is directed along a diagonal with respect to the Ti-O bonds (or the surface normal), similar as in the orthorhombic or rhombohedral phases of bulk BaTiO₃³⁹.

The temperature dependence of the LO₄ edge anomaly is displayed in Fig. 1g, h (the raw spectra are shown in Supplementary Fig. 11), which show that the interfacial polar moments persist to much higher temperature than the field-induced ferroelectric order in bulk STO¹² and vanishes along with the AFD domain boundaries near $T^* = 105\text{ K}$.

Oxygen vacancy clustering scenario. A scenario which can account for the above described asymmetric and non-collinear interfacial polar moment, \mathbf{P} , and its close link with the AFD

domain boundaries of STO is discussed in the following and sketched in Fig. 2. Here, the positively charged oxygen vacancies are assumed to migrate in response to the gate voltage whereby they tend to get trapped and form clusters at the AFD domain boundaries, which act as extended pinning centers (that are likely strengthened/weakened at $-V/+V$). In addition, the AFD domain boundaries may become mobile under a gate voltage⁴⁰ and thus accumulate oxygen vacancies as they move along the interface. An important role is also played by the two-dimensional electron gas (2DEG) whose electrons can get trapped at the oxygen vacancy clusters and thereby reduce their effective charge and the resulting local electric fields. Such a trapping/detrapping of the 2DEG electrons at the oxygen vacancies, and in particular, at the AFD domain boundaries has been observed in recent transport experiments and calculations^{41–46}. The local electric field in the vicinity of the interface is therefore determined by the interplay between the electromigration and clustering of the positive oxygen vacancies at the AFD domain boundaries on the one hand and the trapping/detrapping of some of the 2DEG electrons on the other hand.

In the pristine state, i.e. before any gate voltage has been applied, the oxygen vacancies are more or less randomly distributed and probably weakly pinned at some local defects (see Fig. 2b). Accordingly, the ellipsometry data taken in this pristine state do not show any sign of the R-mode splitting. As a

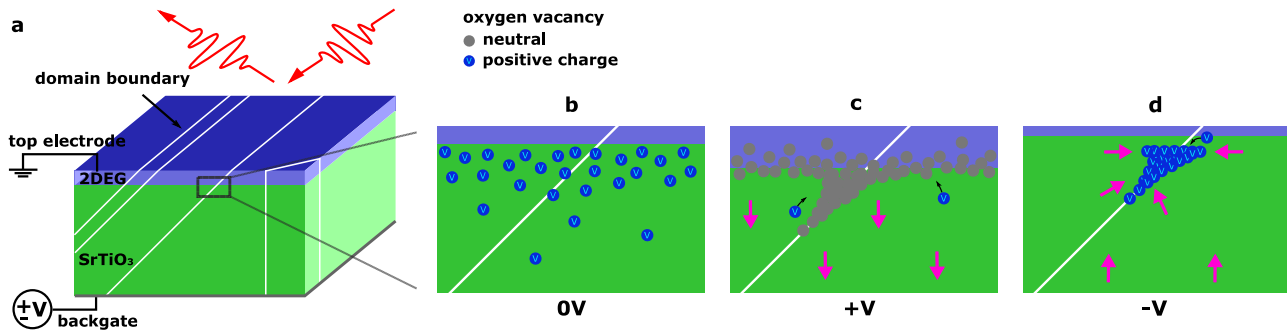


Fig. 2 Schematic of the interfacial electric field. **a** Sketch of a SrTiO₃-based heterostructure and the gating between the grounded two-dimensional electron gas (2DEG) and a backside contact. White lines show the antiferrodistortive (AFD) domain boundaries that develop below the AFD transition at $T^* \approx 105$ K. **b** Magnified view of the interfacial region at 0 V with the 2DEG (purple shading) and positively charged oxygen vacancies (blue dots) that accumulate near the interface but are still randomly distributed. **c** At positive gate bias (+V), the positively charged oxygen vacancies migrate toward the interface and cluster at the AFD domain boundaries. Concurrently, the 2DEG expands and some of the electrons get trapped by the oxygen vacancies which become charge neutral (gray dots). The induced polarization (magenta arrows) is perpendicular to the interface. **d** At negative backgate voltage (−V), the 2DEG is more strongly confined to the interface and the electrons get detrapped from the oxygen vacancies which thus regain a positive charge. The local fields have now a strong horizontal component.

positive gate voltage is first applied (see Fig. 2c), the oxygen vacancies move toward the interface and start accumulating at the AFD domain boundaries. A positive charging of the AFD domain boundaries is, however, counteracted by the trapping of some of the 2DEG electrons which are less strongly confined at +V. The AFD domain boundaries therefore remain (mostly) charge neutral and do not cause local electric fields that give rise to anomalous polar moments. At large +V, the polarization (magenta arrows) thus has a predominant vertical orientation and develops at a distance away from the interface that exceeds the probe depth of the infrared ellipsometry experiment (of about one micrometer, as shown in Supplementary Fig. 12). As the positive gate voltage is subsequently reduced and the electrons start to get detrapped from the oxygen clusters, the effective positive charge of the AFD domain boundaries increases and the local electric field eventually overcomes the threshold for inducing a polar moment. The onset of the induced polar moment \mathbf{P} and the related R-mode splitting thus occurs already on the positive side of the gate voltage loop. Towards the negative side of the gate voltage loop (see Fig. 2d), the R-mode splitting keeps increasing since more oxygen vacancies get trapped at the AFD domain boundaries (as they migrate away from the interface or get accumulated by the moving AFD domain walls) whereas the electrons are more strongly confined to the interface and thus remain detrapped from the oxygen vacancy clusters. On the returning part of the first gate voltage cycle (toward +V), \mathbf{P} and the related magnitude of the R-mode splitting therefore exhibit a clear hysteresis with a higher remnant value at 0 V and a larger coercive field on the +V side, as compared to the first half of the voltage cycle (toward −V).

Note that at large −V the 2DEG may also become laterally inhomogeneous⁴⁷ and thus may further enhance the above described local electric fields (see Supplementary Fig. 16).

From the sketch in Fig. 2 it is evident that the direction of the induced polar moments depends on the type of domain boundaries, i.e. \mathbf{P} is mainly laterally oriented for the boundaries between the x- and y-domains (denoted as x/y-boundaries) whereas it is at 45 degrees with respect to the surface normal ($\mathbf{P}_{ab} \approx \mathbf{P}_c$) for the x/z- and y/z-boundaries⁴⁰. The above described results, which indicate that \mathbf{P}_{ab} and \mathbf{P}_c are of similar magnitude but also strongly depth dependent, are thus consistent with a preferred clustering of the oxygen vacancies at the x/z- and y/z-boundaries as it is sketched in Fig. 2b–d. However, they do not enable a quantitative analysis and are therefore still consistent

with an additional contribution from the x/y boundaries that may arise if in response to the vertical gate field they are moving along the lateral direction, as was reported in ref. 40.

Note that flexoelectric fields due to the strain gradient at the AFD domain boundaries^{19,48} may provide an additional contribution to the local electric field in the vicinity of the interface that is not considered in the above described scenario. This strain gradient can have a significantly different magnitude depending on whether the oxygen vacancy clusters are charge neutral or positively charged and thus become much larger at −V than at +V.

Raman spectroscopy. Complementary information on the gate-voltage-induced polar moments has been obtained with confocal Raman spectroscopy, which has a larger probing depth than infrared ellipsometry and enables scans of the polarization depth profile^{49,50}. Figure 3a shows a sketch of the Raman experiment in grazing incidence geometry with the sample mounted on a wedged holder. The red laser beam ($\lambda = 633$ nm) is incident at 70° to the surface normal and the refracted beam inside STO with $n \approx 2$ is near 30°^{51,52}. The electric field vector ϵ of the light has therefore a sizeable (zero) vertical component in p-polarization (s-polarization).

Figure 3b shows the Raman spectra of AlO_x/STO at 10 K with incoming p-polarization at 0 V and ±4 kV/cm. The background with several broad maxima, arising from multi-phonon excitations, is characteristic for STO (e.g.^{5,53,54}) and hardly affected by the gate voltage. At 0 V (black line), the direct phonon excitations are due to R-modes at 15, 45, 144, 229 and 447 cm^{−1} (black stars) that become Raman-active below $T^* = 105$ K (the cubic phase has no Raman-active phonons)^{4,5,53}. At ±4 kV/cm, several additional peaks develop around 25, 175, 540 and 795 cm^{−1} (green arrows) which correspond to the infrared-active TO₁, TO₂, TO₄ and LO₄ modes (the TO₃ peak at ~263 cm^{−1} is barely resolved) that are activated by a polar distortion which breaks the inversion symmetry⁵⁴.

Figure 3c magnifies the low-energy range with the TO₁ soft mode that exhibits the largest field-effect. The inset shows corresponding s-polarized spectra (normalized to the multi-phonon background) for which the soft mode intensity is significantly weaker. Considering that the Raman intensity of the soft mode is expected to be maximal for $\epsilon \parallel \mathbf{P}$ and minimal (but finite) for $\epsilon \perp \mathbf{P}$, the polarization dependence in Fig. 3c is

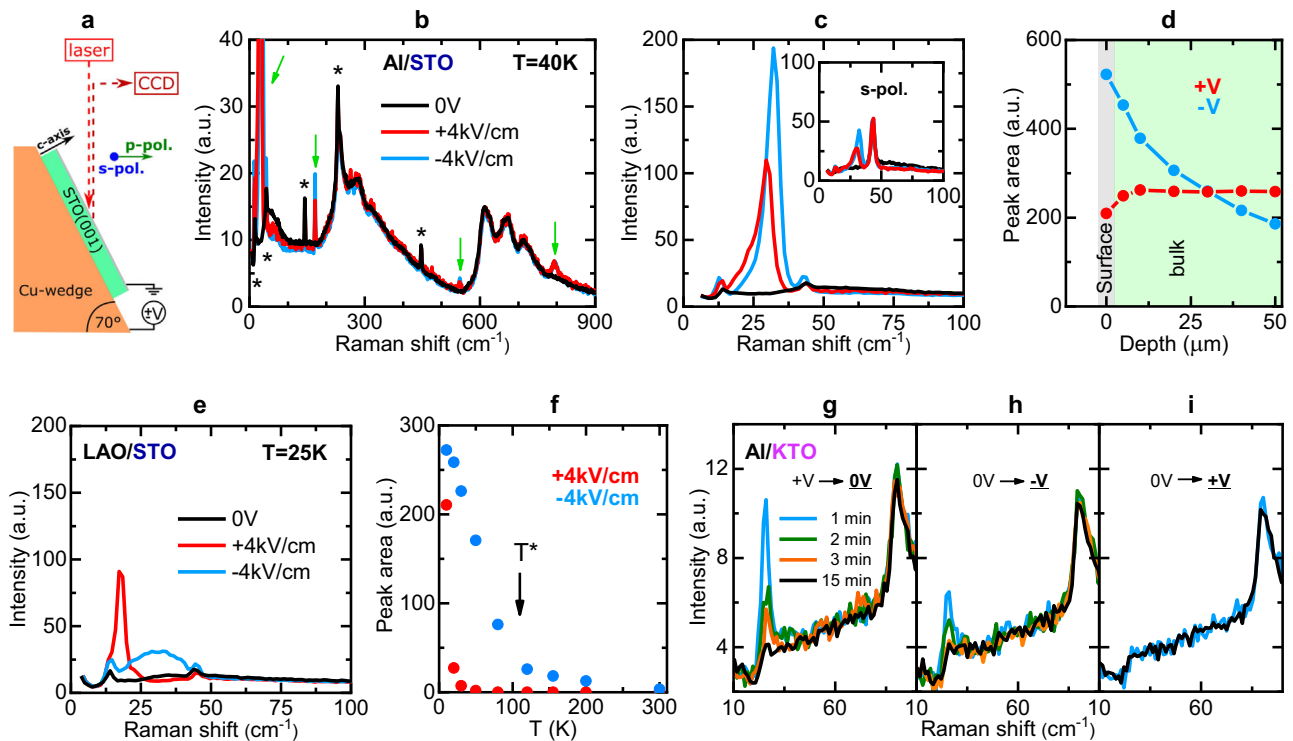


Fig. 3 Confocal Raman spectroscopy study of the induced polar moment. **a** Sketch of the measurement geometry. **b** Gate-voltage-dependent spectra of an $\text{AlO}_x/\text{SrTiO}_3$ heterostructure at 10 K. A Stokes/Anti-Stokes comparison yields a temperature offset of max. ~ 20 K, caused by laser heating. Black stars mark the R-modes at 15, 45, 144, 229 and 447 cm^{-1} that become Raman-active below the antiferrodistortive transition temperature $T^* = 105$ K. Green arrows show the field-induced infrared-active phonon modes at 25, 175, 540 and 795 cm^{-1} . **c** Magnified view of the field-induced soft mode (TO_1) and its asymmetry with respect to $\pm V$. Inset: Corresponding spectra taking in s-polarization (normalized to the multi-phonon background). **d** Depth profile of the normalized peak area of the soft mode for $+V$ and $-V$. **e** Field-dependence of the soft mode of a $\text{LaAlO}_3/\text{SrTiO}_3$ heterostructure. **f** Temperature dependence of the peak area of the soft mode for $+V$ and $-V$. **g-i** Low-frequency Raman spectra of an $\text{AlO}_x/\text{KTaO}_3$ (KTO) heterostructure, showing a weak and rapidly decaying (within minutes) soft mode signal that occurs only after the voltage has been decreased, i.e. either from $+V$ to 0 V (**g**) or from 0 V to $-V$ (**h**), but is absent after a corresponding voltage increase from 0 V to $+V$ or from $-V$ to 0 V (**i**).

therefore consistent with the above described scenario of induced polar moments that are oriented along the diagonal (vertical) direction at -4 kV/cm ($+4\text{ kV/cm}$). Note that a quantitative analysis with respect to the orientation of \mathbf{P} would require a more extensive polarization study and a lateral scanning, as to resolve individual domains with different orientation of \mathbf{P} , which is beyond the scope of this study.

Next, we discuss the depth dependence of the soft mode intensity at $\pm 4\text{ kV/cm}$ in Fig. 3d. At $+4\text{ kV/cm}$, the soft mode intensity shows only a weak variation that agrees with the scenario of a vertical and laterally homogeneous polarization that extends deep into the STO substrate (see Fig. 2c). Close to the interface, the soft mode intensity exhibits a noticeable decrease that is consistent with the absence of an R-mode splitting in the ellipsometry spectra (see Fig. 1a, c), due to the enhanced 2DEG layer and decharged oxygen vacancies. The circumstance that this decrease is only partial can be understood in terms of the probe depth of the confocal Raman experiment, which is on the order of several micrometers and therefore larger than for infrared spectroscopy.

The corresponding depth scan at -4 kV/cm highlights a markedly different trend. Here, the soft mode intensity is strongly enhanced at the interface but decreases rapidly toward the bulk of STO, where it becomes comparable to the one at $+V$. Similar soft mode intensities at $\pm V$ in the bulk of STO are also seen in a conventional macro-Raman experiment that probes deep into the STO substrate (see Supplementary Note 8). These characteristic differences in the depth profile of the gate-voltage-induced

polarization agree with the scenario sketched in Fig. 2d. At $-V$, the polar moments close to the interface are strongly enhanced by the local fields due to the charged AFD domain boundaries and, in addition, are barely screened by the depleted 2DEG.

Figure 3c, e show a comparison of the gate-voltage-induced Raman soft modes of the AlO_x/STO and LAO/STO heterostructures. Whereas the field-induced soft mode peaks are similar for both samples at $+4\text{ kV/cm}$ (red curves), they are dramatically different at -4 kV/cm (cyan curves) where the peak is much stronger and sharper in AlO_x/STO than in LAO/STO . This trend can be understood in terms of the higher oxygen vacancy concentration in AlO_x/STO , which gives rise to larger clusters at the AFD domain boundaries and, correspondingly, to stronger local electric field effects. The mobility of the oxygen vacancies might also depend on the strain that is imposed by the top layer. For the amorphous AlO_x layer, the strain is weakly tensile and thus more favorable for creating large oxygen vacancy clusters than the strongly compressive strain of the epitaxial LAO layer.

Another difference between the induced polarizations at $\pm 4\text{ kV/cm}$ is evident in Fig. 3f which shows the temperature dependence of the Raman soft mode intensity (for LAO/STO). At $+4\text{ kV/cm}$, the soft mode intensity decreases rapidly and vanishes above 40 K , in accordance to the electric-field-induced ferroelectric order in bulk STO¹². The soft mode at -4 kV/cm , however, persists to about $T^* = 105\text{ K}$ where it vanishes together with the AFD domain boundaries. The weak signal above T^* likely arises from remnant AFD surface domains that persist well above T^* ⁵⁵.

Figure 3g–i show a corresponding Raman study of an AlO_x/KTO (001) heterostructure which corroborates the central role of the AFD domain boundaries in the above described interfacial polarization phenomena of the STO-based structures. KTO (KTO) is also a quantum paraelectric with a diverging ϵ_0 at low temperature, albeit not as close to the ferroelectric critical point as STO ^{56,57}. Further, KTO remains in the cubic structure down to the lowest temperature and is therefore void of any AFD domains, and thus does not have an infrared-active R-mode (see Supplementary Fig. 18). The KTO -based devices also host a 2DEG^{58–61} that can be modified with a back-gate voltage, although with less pronounced carrier localization effects at $-V$ than in the STO devices⁶². Figure 3g–i show that in the Raman spectra of AlO_x/KTO the back-gate voltage induces only a weak and short-lived soft mode peak. The metastable soft mode vanishes within minutes and has similar intensities in s- and p-polarization (see Supplementary Fig. 19). Importantly, the soft mode peak is induced only after the gate voltage has been decreased, i.e. after reducing the field from $+8$ kV/cm to 0 V or from 0 V to -8 kV/cm, but not after an increase from -8 kV/cm to 0 V or from 0 V to $+8$ kV/cm. This behavior is consistent with the oxygen vacancies becoming weakly pinned by some local defects, which, unlike the AFD domain boundaries of STO , are not extended and oriented along particular directions. In return, this highlights the central role of the AFD domain boundaries for the asymmetric and non-collinear polarization behavior of the STO -based devices.

UV illumination. Figure 4 demonstrates that the anomalous interfacial polarization of an AlO_x/STO device can be readily modified with other external stimuli, such as UV light. Figure 4a reveals that the splitting of the R-mode in the ellipsometry spectra at -8 kV/cm (cyan line) can be fully suppressed upon UV illumination (violet line) and remains almost completely absent even after the UV light has been switched off (orange line). The original R-mode splitting can be restored by cycling the gate voltage to $+8$ kV/cm (red line) and then back to -8 kV/cm (dark blue line). Figure 4c confirms that the same kind of optical ‘switch-off’ effect occurs for the gate-field-induced anomaly at the LO_4 edge. The underlying mechanism may involve photo-generated electrons that are excited across the bandgap or released from trapping sites and get preferentially trapped at the oxygen vacancy clusters. The accelerated movement of oxygen vacancies may also contribute to this phenomenon.

Figure 4b, d demonstrate that the UV light can also erase the remnant polarization (and thus the memory) at 0 V after a complete electric field cycle. We expect that this demonstration of an electric ‘switch on’ and optical ‘switch off’ mechanism of the interfacial polarization is only one of potentially many examples of how the local and extended defects of STO and their interplay with the 2DEG can be used for engineering STO -based devices with improved or new functionalities (see e.g. ref. ⁶³). Further promising candidates are external pressure, internal strain, chemical substitution, doping and different surface cuts of STO .

Conclusions

In summary, with infrared ellipsometry and confocal Raman spectroscopy we have shown that electric back-gating of LAO/STO and AlO_x/STO heterostructures gives rise to interfacial polar moments that are non-collinear and strongly asymmetric with respect to the vertical gate field. Our results provide evidence for an important role of oxygen vacancies which tend to form extended clusters at the AFD domain boundaries that give rise to electric charging effects. The subsequent interfacial polar moments with large horizontal components are induced at lower

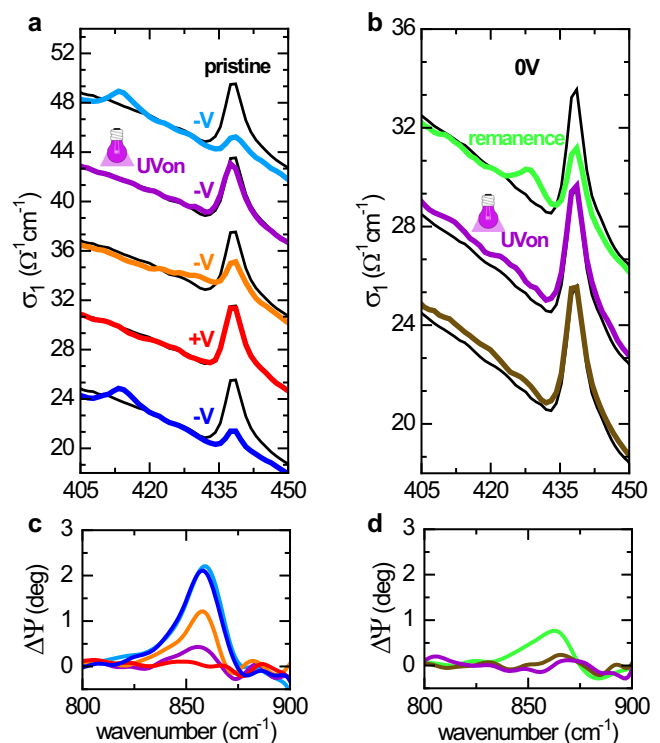


Fig. 4 Optical switching of the anomalous polarization in $\text{AlO}_x/\text{SrTiO}_3$ at **10 K**. **a** Infrared spectra showing that the pronounced R-mode splitting at -8 kV/cm (cyan) can be erased by UV illumination (violet) and is only partially restored after the illumination (orange). The original R-mode splitting is restored after a field cycle to $+8$ kV/cm (red) and back to -8 kV/cm (blue). **b** Infrared spectra at 0 V showing that the remnant R-mode splitting (green) is erased by the UV light (violet) even after it has been turned off again (brown). **c, d** Corresponding infrared spectra of the polarization-induced TO mode at the LO_4 edge. Shown are the difference spectra of the ellipsometric angle Ψ with respect to the pristine state at 0 V, i.e. $\Delta\Psi = \Psi_{\text{exp}} - \Psi_{0\text{V, pristine}}$. The data are smoothed with a FFT filter.

gate voltages and persists to much higher temperatures than in bulk STO .

The training and hysteresis effects due to these anomalous interfacial polar moments are reflected in the magneto-transport properties of related devices^{28,29}. However, since the laterally inhomogeneous polarization effects tend to be cancelled out in vertical structures, their real potential can only be exploited with lateral device structures. Recently, there have been great advances in patterning ferroelectric domains⁶⁴ which may also be effective in STO due to its polar nature. Our work contributes to the understanding of the mechanisms underlying those experiments, and will offer opportunities to design electronic devices harnessing ferroelastic domain walls in STO 2DEGs, by controlling AFD domain boundaries and their interaction with oxygen vacancies.

Methods

Infrared ellipsometry. The infrared ellipsometry measurements were performed in the rotating analyzer ellipsometer (RAE) configuration, with the angle of incidence being close to the Brewster angle of 75 degrees. The measured quantities are the amplitude-ratio Ψ of the Fresnel coefficients and the relative phase shift between the reflected s- and p-polarized light, Δ . The optical setup consists of a Bruker 70 v Fast-Fourier spectrometer, which is attached to a home-built setup and equipped with a Helium-flow cryostat, allowing a temperature variation of 5 – 300 K. In order to apply back-gate voltages of up to 400 Volt, the samples were electrically wired as sketched in Fig. 2a. Here, the top electrode is the two-dimensional electron gas formed at the SrTiO_3 or KTO interface and connected via four wires with the ground. The backside of the sample is pasted with silver paint onto a ceramic plate for electrical insulation. In addition, the sample surface can be in-situ illuminated with UV light emitted from a 100 Watt Xenon lamp,

which covers a broad energy range of 1.2–6.2 eV. For the dark measurements without UV-illumination, the samples were entirely shielded against visible and UV light in order to avoid photodoping effects.

Confocal Raman spectroscopy. The confocal Raman spectra were recorded on a commercial HORIBA LabRAM HR800 spectrometer using the 632.8 nm excitation line of a HeNe laser in full backscattering geometry and visualized with the software LabSpec. A small confocal hole of 50 μm in diameter suppresses the back-scattered light from out-of-focus regions of the sample (see Supplementary Fig. 13b), which results in a spatial resolution of a few micrometers in vertical direction. A high-precision stage enables the depth-dependent measurements by changing the focus position of the laser light in vertical direction with an accuracy of 0.5 μm . The laser light was focused with a $\times 100$ long-working distance objective with a short depth of focus, $\text{NA} = 0.6$, resulting in laser powers of <1 mW on the sample. Laser heating effects were considered by the comparison of the Anti-Stokes with the Stokes signal via the Bose-Einstein relation, which yields a maximal temperature offset of ~ 20 K (see Supplementary Note 7). The sample is placed on a Cu-wedge of 70 degrees (see Fig. 3a and Supplementary Fig. 13a). This configuration allows the detection of in-plane and out-of-plane contributions of the optical response by changing the polarization of the incoming laser light. The backgate voltages experiments as a function of temperature were performed in analogy to the infrared ellipsometry measurements, with the exception that here a sapphire plate was used instead of a ceramic plate, due to its high thermal but low electrical conductance. All reported spectra have been corrected considering the Bose thermal factor.

Data availability

The data used in this manuscript are available from the corresponding author upon request.

Received: 31 August 2021; Accepted: 5 May 2022;

Published online: 30 May 2022

References

- Cardona, M. "Optical Properties and Band Structure of SrTiO_3 and BaTiO_3 ," *Phys. Rev.* **140**, A651–A655 (1965).
- Benthem, K., Elsässer, C. & French, R. H. "Bulk electronic structure of SrTiO_3 : Experiment and theory," *J. Appl. Phys.* **90**, 6156–6164 (2001).
- De Souza, R. A., Fleig, J., Merkle, R. & Maier, J. "SrTiO₃: A Model Electroceramic," *Z. für Metallkd.* **94**, 218–225 (2003).
- Fleury, P. A., Scott, J. F. & Worlock, J. M. "Soft Phonon Modes and the 110 °K Phase Transition in SrTiO_3 ," *Phys. Rev. Lett.* **21**, 16–19 (1968).
- Petzelt, J. et al. "Dielectric, infrared, and Raman response of undoped SrTiO_3 ceramics: Evidence of polar grain boundaries," *Phys. Rev. B* **64**, 184111 (2001).
- Salje, E. K. H., Aktas, O., Carpenter, M. A., Laguta, V. V. & Scott, J. F. "Domains within Domains and Walls within Walls: Evidence for Polar Domains in Cryogenic SrTiO_3 ," *Phys. Rev. Lett.* **111**, 247603 (2013).
- He, L. & Vanderbilt, D. "First-principles study of oxygen-vacancy pinning of domain walls in PbTiO_3 ," *Phys. Rev. B* **68**, 134103 (2003).
- Van Aert, S. et al. "Direct Observation of Ferrielectricity at Ferroelastic Domain Boundaries in CaTiO_3 by Electron Microscopy," *Adv. Mater.* **24**, 523–527 (2012).
- Zubko, P., Catalan, G., Buckley, A., Welche, P. R. L. & Scott, J. F. "Strain-Gradient-Induced Polarization in SrTiO_3 Single Crystals," *Phys. Rev. Lett.* **99**, 167601 (2007).
- Müller, K. A. & Burkard, H. "SrTiO₃: An intrinsic quantum paraelectric below 4 K," *Phys. Rev. B* **19**, 3593–3602 (1979).
- Vogt, H. "Refined treatment of the model of linearly coupled anharmonic oscillators and its application to the temperature dependence of the zone-center soft-mode frequencies of KTaO_3 and SrTiO_3 ," *Phys. Rev. B* **51**, 8046–8059 (1995).
- Hemberger, J. et al. "Quantum paraelectric and induced ferroelectric states in," *J. Phys. Condens. Matter* **8**, 4673–4690 (1996).
- Bednorz, J. G. & Müller, K. A. " $\text{Sr}_{1-x}\text{Ca}_x\text{TiO}_3$: An XY Quantum Ferroelectric with Transition to Randomness," *Phys. Rev. Lett.* **52**, 2289–2292 (1984).
- Rischau, C. W. et al. "A ferroelectric quantum phase transition inside the superconducting dome of $\text{Sr}_{1-x}\text{Ca}_x\text{TiO}_3-\delta$," *Nat. Phys.* **13**, 643–648 (2017).
- Haeni, J. H. et al. "Room-temperature ferroelectricity in strained SrTiO_3 ," *Nature* **430**, 758–761 (2004).
- Uwe, H. & Sakudo, T. "Stress-induced ferroelectricity and soft phonon modes in SrTiO_3 ," *Phys. Rev. B* **13**, 271–286 (1976).
- Fleury, P. A. & Worlock, J. M. "Electric-Field-Induced Raman Scattering in SrTiO_3 and KTaO_3 ," *Phys. Rev.* **174**, 613–623 (1968).
- Itoh, M. et al. "Ferroelectricity Induced by Oxygen Isotope Exchange in Strontium Titanate Perovskite," *Phys. Rev. Lett.* **82**, 3540–3543 (1999).
- Zubko, P., Catalan, G. & Tagantsev, A. K. "Flexoelectric Effect in Solids," *Annu. Rev. Mater. Res.* **43**, 387–421 (2013).
- Seidel, J. et al. "Conduction at domain walls in oxide multiferroics," *Nat. Mater.* **8**, 229–234 (2009).
- Leighton, C. "Electrolyte-based ionic control of functional oxides," *Nat. Mater.* **18**, 13–18 (2019).
- Caviglia, A. D. et al. "Electric field control of the $\text{LaAlO}_3/\text{SrTiO}_3$ interface ground state," *Nature* **456**, 624–627 (2008).
- Ohtomo, A. & Hwang, H. Y. "A high-mobility electron gas at the $\text{LaAlO}_3/\text{SrTiO}_3$ heterointerface," *Nature* **427**, 423–426 (2004).
- Nakagawa, N., Hwang, H. Y. & Muller, D. A. "Why some interfaces cannot be sharp," *Nat. Mater.* **5**, 204–209 (2006).
- Thiel, S., Hammerl, G., Schmehl, A., Schneider, C. W. & Mannhart, J. "Tunable Quasi-Two-Dimensional Electron Gases in Oxide Heterostructures," *Science* **313**, 1942–1945 (2006).
- Reyren, N. et al. "Superconducting Interfaces Between Insulating Oxides," *Science* **317**, 1196–1199 (2007).
- Chen, Y. Z. et al. "A high-mobility two-dimensional electron gas at the spinel/perovskite interface of $\gamma\text{-Al}_2\text{O}_3/\text{SrTiO}_3$," *Nat. Commun.* **4**, 1371 (2013).
- Noël, P. et al. "Non-volatile electric control of spin-charge conversion in a SrTiO_3 Rashba system," *Nature* **580**, 483–486 (2020).
- Vaz, D. C. et al. "Mapping spin-charge conversion to the band structure in a topological oxide two-dimensional electron gas," *Nat. Mater.* **18**, 1187–1193 (2019).
- Trier, F. et al. "Electric-Field Control of Spin Current Generation and Detection in Ferromagnet-Free SrTiO_3 -Based Nanodevices," *Nano Lett.* **20**, 395–401 (2020).
- Herranz, G. et al. "High Mobility in $\text{LaAlO}_3/\text{SrTiO}_3$ Heterostructures: Origin, Dimensionality, and Perspectives," *Phys. Rev. Lett.* **98**, 216803 (2007).
- Kalabukhov, A. et al. "Effect of oxygen vacancies in the SrTiO_3 substrate on the electrical properties of the $\text{LaAlO}_3/\text{SrTiO}_3$ interface," *Phys. Rev. B* **75**, 121404 (2007).
- Rödel, T. C. et al. "Universal Fabrication of 2D Electron Systems in Functional Oxides," *Adv. Mater.* **28**, 1976–1980 (2016).
- Casals, B. et al. "Low-Temperature Dielectric Anisotropy Driven by an Antiferroelectric Mode in SrTiO_3 ," *Phys. Rev. Lett.* **120**, 217601 (2018).
- Rössle, M. et al. "Electric-Field-Induced Polar Order and Localization of the Confined Electrons in $\text{LaAlO}_3/\text{SrTiO}_3$ Heterostructures," *Phys. Rev. Lett.* **110**, 136805 (2013).
- Azzam, R., Bashara, N. & Burns, D. "Ellipsometry and polarized light : North Holland, Amsterdam, 1987 (ISBN 0-444-87016-4). xvii + 539 pp. Price Dfl. 75.00," *Analytica Chim. Acta* **199**, 283–284 (1987).
- Schubert, M., Infrared Ellipsometry on Semiconductor Layer Structures, G. Höhler, Ed., Springer (2004).
- Bernhard, C., Humlíček, J. & Keimer, B. "Far-infrared ellipsometry using a synchrotron light source—the dielectric response of the cuprate high Tc superconductors," *Thin Solid Films* **455–456**, 143–149 (2004).
- Potnis, P. R., Tsou, N.-T. & Huber, J. E. "A Review of Domain Modelling and Domain Imaging Techniques in Ferroelectric Crystals," *Materials* **4**, 417–447 (2011).
- Honig, M. et al. "Local electrostatic imaging of striped domain order in $\text{LaAlO}_3/\text{SrTiO}_3$," *Nat. Mater.* **12**, 1112–1118 (2013).
- Delahaye, J. & Grenet, T. "Metallicity of the SrTiO_3 surface induced by room temperature evaporation of alumina," *J. Phys. D: Appl. Phys.* **45**, 315301 (2012).
- Krantz, P. W. & Chandrasekhar, V. "Observation of Zero-Field Transverse Resistance in $\text{AlO}_x/\text{SrTiO}_3$ Interface Devices," *Phys. Rev. Lett.* **127**, 036801 (2021).
- Zurhelle, A. F., Christensen, D. V., Menzel, S. & Gunkel, F. "Dynamics of the spatial separation of electrons and mobile oxygen vacancies in oxide heterostructures," *Phys. Rev. Mater.* **4**, 104604 (2020).
- Yin, C. et al. "Electron Trapping Mechanism in $\text{LaAlO}_3/\text{SrTiO}_3$ Heterostructures," *Phys. Rev. Lett.* **124**, 017702 (2020).
- Ojha, S. K. et al. "Electron Trapping and Detrapping in an Oxide Two-Dimensional Electron Gas: The Role of Ferroelastic Twin Walls," *Phys. Rev. Appl.* **15**, 054008 (2021).
- Frenkel, Y. et al. "Imaging and tuning polarity at SrTiO_3 domain walls," *Nat. Mater.* **16**, 1203–1208 (2017).
- Kalisky, B. et al. "Locally enhanced conductivity due to the tetragonal domain structure in $\text{LaAlO}_3/\text{SrTiO}_3$ heterointerfaces," *Nat. Mater.* **12**, 1091–1095 (2013).
- Gong, W. et al. "Oxygen-deficient SrTiO_3-x , $x = 0.28, 0.17$, and 0.08 . Crystal growth, crystal structure, magnetic, and transport properties," *J. Solid State Chem.* **90**, 320–330 (1991).
- Hepting, M. et al. "Tunable Charge and Spin Order in PrNiO_3 Thin Films and Superlattices," *Phys. Rev. Lett.* **113**, 227206 (2014).

50. Lyzwa, F. et al. "Backfolded acoustic phonons as ultrasonic probes in metal-oxide superlattices," *Phys. Rev. Mater.* **4**, 043606 (2020).
51. Rössle, M. et al. "Optical probe of ferroelectric order in bulk and thin-film perovskite titanates," *Phys. Rev. B* **88**, 104110 (2013). 9.
52. Lyzwa, F. et al. "In situ monitoring of atomic layer epitaxy via optical ellipsometry," *J. Phys. D: Appl. Phys.* **51**, 125306 (2018).
53. Gray, D. J., Merz, T. A., Hikita, Y., Hwang, H. Y. & Mabuchi, H. "Orientation-resolved domain mapping in tetragonal SrTiO_3 using polarized Raman spectroscopy," *Phys. Rev. B* **94**, 214107 (2016).
54. Akimov, I. A., Sirenko, A. A., Clark, A. M., Hao, J.-H. & Xi, X. X. "Electric-Field-Induced Soft-Mode Hardening in SrTiO_3 Films," *Phys. Rev. Lett.* **84**, 4625–4628 (2000).
55. Mishina, E. D. et al. "Observation of a Near-Surface Structural Phase Transition in SrTiO_3 by Optical Second Harmonic Generation," *Phys. Rev. Lett.* **85**, 3664–3667 (2000).
56. Rowley, S. E. et al. "Ferroelectric quantum criticality," *Nat. Phys.* **10**, 367–372 (2014).
57. Fujishita, H. et al. "Quantum Paraelectric States in SrTiO_3 and KTaO_3 : Barrett Model, Vendik Model, and Quantum Criticality," *J. Phys. Soc. Jpn.* **85**, 074703 (2016).
58. Zou, K. et al. " $\text{LaTiO}_3/\text{KTaO}_3$ interfaces: A new two-dimensional electron gas system," *APL Mater.* **3**, 036104 (2015).
59. Ueno, K. et al. "Discovery of superconductivity in KTaO_3 by electrostatic carrier doping," *Nat. Nanotechnol.* **6**, 408–412 (2011).
60. Zhang, H. et al. "Highly Mobile Two-Dimensional Electron Gases with a Strong Gating Effect at the Amorphous $\text{LaAlO}_3/\text{KTaO}_3$ Interface," *ACS Appl. Mater. Interfaces* **9**, 36456–36461 (2017).
61. Zhang, H. et al. "Unusual Electric and Optical Tuning of KTaO_3 -Based Two-Dimensional Electron Gases with 5d Orbitals," *ACS Nano* **13**, 609–615 (2019).
62. Chen, Z. et al. "Two-Dimensional Superconductivity at the $\text{LaAlO}_3/\text{KTaO}_3(110)$ Heterointerface," *Phys. Rev. Lett.* **126**, 026802 (2021).
63. Chen, Y. et al. "Photoinduced Persistent Electron Accumulation and Depletion in $\text{LaAlO}_3/\text{SrTiO}_3$ Quantum Wells," *Phys. Rev. Lett.* **124**, 246804 (2020).
64. Li, D. & Bonnell, D. A. "Controlled Patterning of Ferroelectric Domains: Fundamental Concepts and Applications," *Annu. Rev. Mater. Res.* **38**, 351–368 (2008).

Acknowledgements

F.L. and C.B. acknowledge enlightening discussions with S. Das, J. Maier, R. Merkle, A. Dubroka, and B. I. Shklovskii. Work at the University of Fribourg was supported by the Schweizerische Nationalfonds (SNF) by Grant No. 200020-172611. M.B. acknowledges support from the ERC Advanced grant n° 833973 "FRESCO" and the QUANTERA project "QUANTOX". G.H. acknowledges financial support from Spanish Ministry of Science and Innovation (MCIN/AEI/10.13039/501100011033) through the Severo Ochoa

FUNFUTURE (CEX2019-000917-S) and Grant No. PID2020-118479RB-I00, and Generalitat de Catalunya (2017 400 SGR 1377).

Author contributions

F.L. performed and analyzed the infrared ellipsometry measurements under the direction of P.M., M.Y.-R., B.X., Y.P. and C.B. The confocal Raman spectroscopy measurements were performed and analyzed by F.L. with the help from M.M., K.F., B.K., B.P.P.M., A.C., A.S., Y.P. and C.B. The macro-Raman measurements were carried out by M.C. and P.H. L.M.V.A., D.C.V., G.H. and M.B. grew the samples and performed the magneto-transport measurements. C.B. and F.L. conceived and planned the project, and wrote the manuscript with inputs from all authors. All authors discussed the results.

Competing interests

The authors declare no competing interests.

Additional information

Supplementary information The online version contains supplementary material available at <https://doi.org/10.1038/s42005-022-00905-3>.

Correspondence and requests for materials should be addressed to Fryderyk Lyzwa or Christian Bernhard.

Peer review information *Communications Physics* thanks the anonymous reviewers for their contribution to the peer review of this work.

Reprints and permission information is available at <http://www.nature.com/reprints>

Publisher's note Springer Nature remains neutral with regard to jurisdictional claims in published maps and institutional affiliations.



Open Access This article is licensed under a Creative Commons Attribution 4.0 International License, which permits use, sharing, adaptation, distribution and reproduction in any medium or format, as long as you give appropriate credit to the original author(s) and the source, provide a link to the Creative Commons license, and indicate if changes were made. The images or other third party material in this article are included in the article's Creative Commons license, unless indicated otherwise in a credit line to the material. If material is not included in the article's Creative Commons license and your intended use is not permitted by statutory regulation or exceeds the permitted use, you will need to obtain permission directly from the copyright holder. To view a copy of this license, visit <http://creativecommons.org/licenses/by/4.0/>.

© The Author(s) 2022